# Online Supplement:

# Small Airway Reduction and Fibrosis is an Early Pathologic Feature of Idiopathic Pulmonary Fibrosis

**Running title:** Small airways disease in IPF

Kohei Ikezoe[1], Tillie-Louise Hackett[1], Samuel Peterson[3], Dante Prins[1], Cameron J. Hague[2], Darra Murphy[2], Stacey LeDoux[1], Fanny Chu[1], Feng Xu[1], Joel D. Cooper[5], Naoya Tanabe[6], Christopher J. Ryerson[1], Peter D. Paré[1], Harvey O. Coxson[1], Thomas V. Colby[4], James C. Hogg[1], and Dragoş M. Vasilescu[1]

[1]Centre for Heart and Lung Innovation, St. Paul's Hospital, University of British Columbia, Vancouver, BC, Canada,

[2]Department of Radiology, University of British Columbia, Vancouver, BC, Canada,

[3]VIDA Diagnostics, Coralville, IA, USA,

[4]Department of Laboratory Medicine and Pathology, Mayo Clinic, Scottsdale, AZ, USA,

[5]Department of Thoracic Surgery, University of Pennsylvania. Philadelphia, PA, USA,

[6]Department of Respiratory Medicine, Graduate School of Medicine, Kyoto University, Kyoto

**Table of contents:**

**Table E1. Diagnostic information of IPF cases**

| Case | CT diagnosis | Histopathology diagnosis | Final clinical diagnosis |
|---|---|---|---|
| 1 | UIP | UIP | IPF |
| 2 | Alternative diagnosis | UIP | IPF |
| 3 | UIP | UIP | IPF |
| 4 | UIP | UIP | IPF |
| 5 | UIP | UIP | IPF |
| 6 | UIP | UIP | IPF |
| 7 | Alternative diagnosis | UIP | IPF |
| 8 | Alternative diagnosis | UIP | IPF |

**Airway skeleton-based measurements**

The small airways in IPF display a high degree of distortion (Figure 5 in main manuscript) potentially caused by the tissue remodeling surrounding the airways. The distortions can be visually described as localized dilatations or constrictions leading to twisted and curved airways. To enable a quantitative assessment of these morphometric changes, it was important to develop new mathematical descriptions of these geometric attributes based on the centerline (skeleton line) of the segmented airways. After all conducting airways as well as the first generation of respiratory bronchioles were segmented, the terminal bronchioles were labeled as the last generation of conducting airways. The skeleton of the whole airway tree was calculated and 11 cross-sections perpendicular to the general direction of the terminal bronchioles were computed along the whole bronchiole branch in 10% increments. Figure E1 provides an overview of the

skeletonization processing and cross-sectional image extraction. The following sections describe the methodology for obtaining cross-sectional images and quantification of degree of distortion of the small airways.

***Computation of airway branch length***

A skeleton line generated from a 3D image segmentation is limited by the resolution (voxel size = pixel length * pixel width * pixel depth) of the original image, as represented by the white dots inside the sub-panel in Figure E1C. This means that each skeleton is a list of discrete points that are connected by lines only for visual appearance. The simple sum of all voxels that form a skeleton is not accurate due to neighboring points being joined in 2 or 3 cartesian directions.

Therefore, to calculate the correct branch length the following formula is implemented:

$$L = \sum_{i=2}^{N} |(\vec{P}_i - \vec{P}_{i-1})| = \sum_{i=2}^{N} \sqrt{(x_i - x_{i-1})^2 + (y_i - y_{i-1})^2 + (z_i - z_{i-1})^2}$$

Where $\vec{P}$ denotes the position of a voxel on the skeleton line as 3D coordinates, which are scaled based on the resolution of the scan. $N$ indicates the total voxel count for the airway, with $i$ denoting index number.

***Computation of cross-sectional images***

Obtaining cross-sectional images in airways from normal subjects or patients with COPD is relatively simple since their airways are generally very straight. However, as visualized in this manuscript, the distortion of airways in IPF patients is highly significant and previous methods of obtaining true cross-sections was not applicable. Therefore, the algorithms for determining branch length and the correct angle of cross-sections had to be revised to address highly distorted airways.

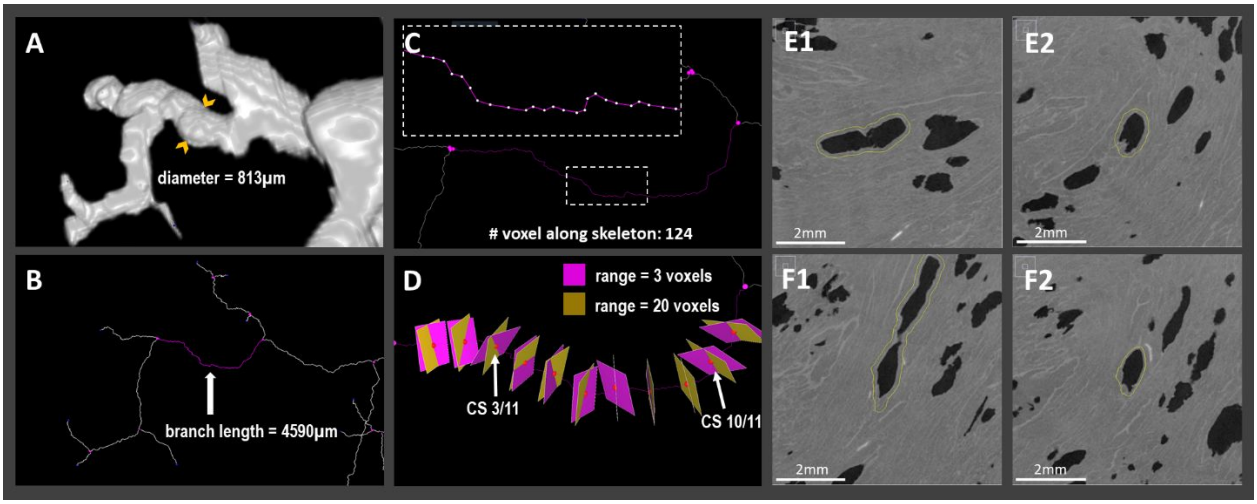


**Figure E1: The process of obtaining cross-sectional images:** (A): A 3D rendering of an airway segmentation generated from the MicroCT scan. (B) One airway branch in the skeleton tree generated from the airways visualized in A is selected (magenta color) and the calculated branch length is shown below. (C) A closer view of the skeleton with annotated voxels (white dots) showing the mathematical basis for the skeleton where a line is interpolated between the points for visual purposes, (D) A 3D depiction of the alignment of cross sections generated from the image, the parameter range concerns the calculation direction for such cross sections, (E) A pair of cross section images generated at the point marked *CS 3/11* in D with the parameter range set to 3 and 20, E1 and E2 respectively. (F) A pair of cross section images generated at the point marked *CS 10/11* in D with the parameter range set to 3 and 20, F1 and F2 respectively.

The goal of cross-sectional image analysis is to obtain true measurements of wall and lumen areas. To minimize the effect of oblique cuts through an airway which would increase wall thicknesses and provide the wrong impression of the airway shape, it is crucial to calculate the correct cross-sectional plane through an airway. Small, localized distortions of the airway skeleton line can lead to the computation of the wrong cross-sectional plane if only a small number of skeleton line points are used.

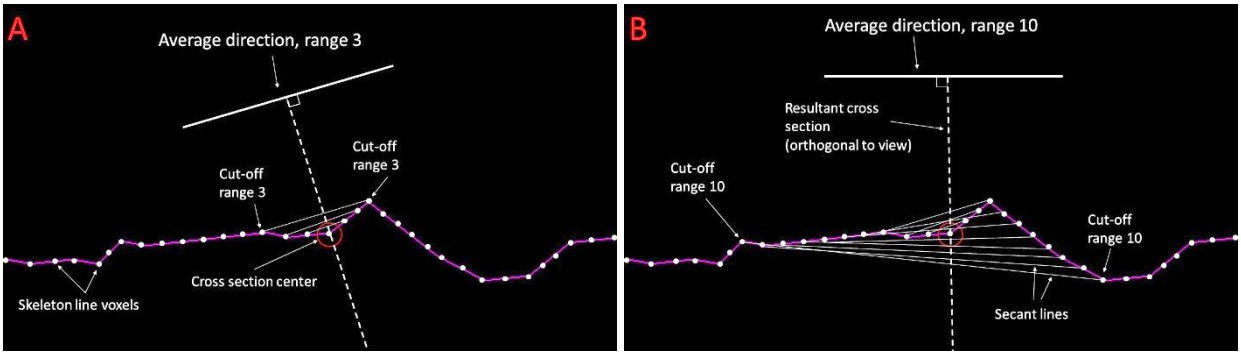


**Figure E2: Example of calculation of cross-section plane based on secant line averaging:** A magnified portion of a skeleton line (purple) represents 1mm of a whole airway branch and is used as an example. Small "bumps" in the skeleton line are caused by noise related imperfections in the airway segmentation and should not be allowed to affect measurements. The discrete skeleton line voxels are depicted by dots (white), with secant lines (white lines) being drawn between the same number of voxels to the left and right of the voxel (circled in red) for which the cross-section should be calculated. (A) Shows the average direction calculated from 3 secant lines. (B) Shows the average direction calculated from 10 secant lines. Resulting cross-section plane (dashed line) is shown in both sub-panels (A and B) for the respective number of secant lines used, highlighting the impact of choosing an appropriate number of points.

A formula was developed from the principle that a cross-section is orthogonal to the path of an airway. Thus, to find the cross-section of a continuous multivariable function a tangent line at the desired point should be used, indicating the instantaneous direction of the skeleton line at that location. A visualization of normal planes based on 3D tangent lines can be performed on the online platform GeoGebra (1). Because of the discrete nature of the skeleton line, a more robust method must be used to find an approximate tangent line. The most immediate solution is the secant line (a straight line intersecting two points on a function) between the two neighboring voxels. However, because of the noise associated with operating at the resolution limit of the microCT scan and the forced discreteness of voxel points of the raw images, it is important to compute the final tangent based on an average of multiple secant lines, as illustrated in Figure E2.

Given a vector $\vec{P}_n$, representing the position of the voxel at which we wish to generate a cross section, secant lines are drawn between neighbors from this center voxel at increasing integers

from 1 to the desired range R, i.e. 20. These secant lines can be seen in Figure E2 as white lines between voxels indicated as dots. The average direction of these secant lines is then calculated as $\vec{V}$ which represents the direction of the skeleton line at the cross-section center seen for two ranges (6 and 20 points) as shown in Figures E2A and E2B.

$$\vec{V} = \sum_{i=1}^{R} (\vec{P}_{n-i} - \vec{P}_{n+i}) = \sum_{i=1}^{R} \langle x_{n-i} - x_{n+i} \,|\, y_{n-i} - y_{n+i} \,|\, z_{n-i} - z_{n+i} \rangle$$

Where $\vec{P}_n$ is a vector representing the 3D position of the central voxel for the cross section, and n is its index. R is the consideration range, the maximum # of voxels to be considered. For airways with a length of <200 voxels, the range of the first and last cross-section will be reduced up to the maximum value possible value given the limits of the voxel count. $\vec{V}$ is a vector that describes the direction of the airway which the orthogonal cross-section plane is then calculated. Using the direction of $\vec{V}$, the angle to rotate the original CT image can be procedurally calculated which we center at $\vec{P}_0$ after the transformation producing the final cross-sectional images.

The value of the consideration range R must be carefully selected (not too large or too small) so that the calculation of the orthogonal plane is not susceptible to minor local inaccuracies, but still accounting for airway curves. To determine a pertinent value of R, manual inspection of the cross-sectional images along with 3D visualizations of the tangent lines were done. From the 3D cross section alignment indicated by colored squares in Figure E1D, a range of R=20 produces cross-sections with a more accurate alignment to the airway's path. In particular, CS3/11 in Figure E1D corresponds to the cross-sections in Figure E1E and CS10/11 to Figure E1F. It was found that a consideration range of 20 in both directions, R=20 gave the more accurate results as shown in Figure E1E2 and E1F2 compared to Figure E1E1 and E1F1 for which a value of R=3

was used. Using a range exceeding 20 was found to reduce the sensitivity to curves in the airway that were flatted out by the long consideration range. In comparison a range less than 20 was found to be susceptible to small variance and noise present at the limits of the image's resolution, as seen in the comparison between a shorter and longer range in Figure E2A and E2B, where the overall curve of the airway is better captured in Figure E2B.

**Quantitative assessment of airway distortions**

The most commonly used metric for evaluating the degree of distortion of a line or a tube such as an airway branch is called tortuosity (2). An equation for tortuosity typically used is $T = \frac{L_p}{L_C}$, where $L_p$ is the length of a path (airway skeleton line) and $L_c$ is the straight line between the start and end point (branch points in an airway tree), denoted c for chord length. An example of this calculation is given in Figure E3A. Tortuosity must always be greater than 1 and depends on the amount of curving and also distortion or "roughness" of the path. However, tortuosity alone cannot be used to differentiate between a path with many small distortions (i.e. rough) and a curved path because it is dependent on both roughness and curviness as depicted in Figure E3B. Therefore, a new formula was constructed that takes tortuosity into account, but accounts for the roughness attribute.

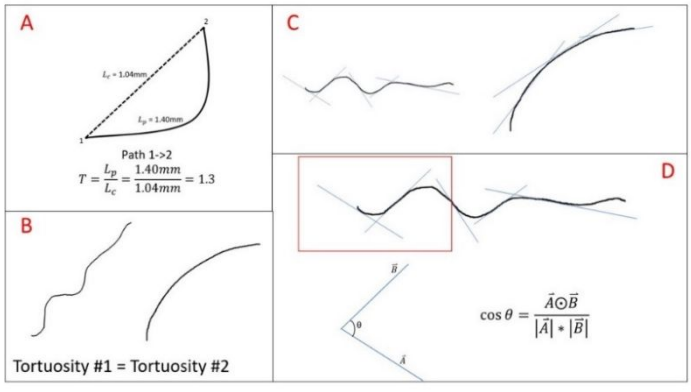


Figure E3: **Visual examples for calculating tortuosity and roughness** (skeleton line are depicted in black). (A) Tortuosity calculation for theoretical example of a curved airway path. (B) Example of two skeleton lines with the same tortuosity. (C) Examples of localized trendlines depicted in blue, are used to calculate curviness. (D) A graphical depiction of the dot product formula and its use to compare two neighboring trendlines $\vec{A}$ and $\vec{B}$ to calculate roughness.

***Roughness***

Roughness is a parameter that can measure rapid, local changes, through the analysis of the direction of neighboring tangents along the airway center line. For straight or slowly curving airways, the direction of the tangent line changes slowly in comparison to jagged, rough airway paths where the tangent change direction rapidly. Because of the discrete nature of the voxels in each skeleton line, the tangent line was replaced with a localized trendline for a small number of voxels (n=7, empirically determined based on variation in 20 unbiasedly selected airways). A diagram of these trendlines is given in Figure E3C to show how the rough airway on the left has rapidly changing trendlines in comparison to the smooth, curving airway on the right. These trendlines are then compared to the neighboring trendlines to the left and right using the dot product formula to determine the cosine of the angle between the two, as depicted in Figure E3D with the two neighboring trendlines $\vec{A}$ and $\vec{B}$.

The formula for $\cos\theta$ is $\cos\theta = \frac{\vec{A}\odot\vec{B}}{|\vec{A}| * |\vec{B}|}$, where $\vec{A}\odot\vec{B}$ is the dot product between two vectors, defined as coordinate multiplication $\vec{A}\odot\vec{B} = x_a * x_b + y_a * y_b + z_a * z_b$ and the length of a vector $|\vec{V}|$ is $|\vec{V}| = \sqrt{x_v^2 + y_v^2 + z_v^2}$. After obtaining the cosine value, the average for each of the comparisons between neighbors is computed and an empirically determined exponent of 7 is added to accentuate sensitivity. The final formula used to calculate the amount of localized distortions (roughness) of each airway branch was:

$$roughness = 1 - mean\left[(\cos\theta)^7\right] = 1 - \frac{\sum_{i=1}^{N-1}(\cos\theta)^7}{N-1} = 1 - \frac{\sum_{i=1}^{N-1}\left(\frac{\vec{T}_i\odot\vec{T}_{i+1}}{|\vec{T}_i| * |\vec{T}_{i+1}|}\right)^7}{N-1}$$

Where $N$ is the number of trendlines, $i$ is the current trendline index and $\vec{T}_i$ is direction of the current trendline.

Based on the examples of potential angles between neighboring trendlines presented in Figure E4, the value of roughness can range between 0 for straight paths to 1 for paths that change direction in a right angle.

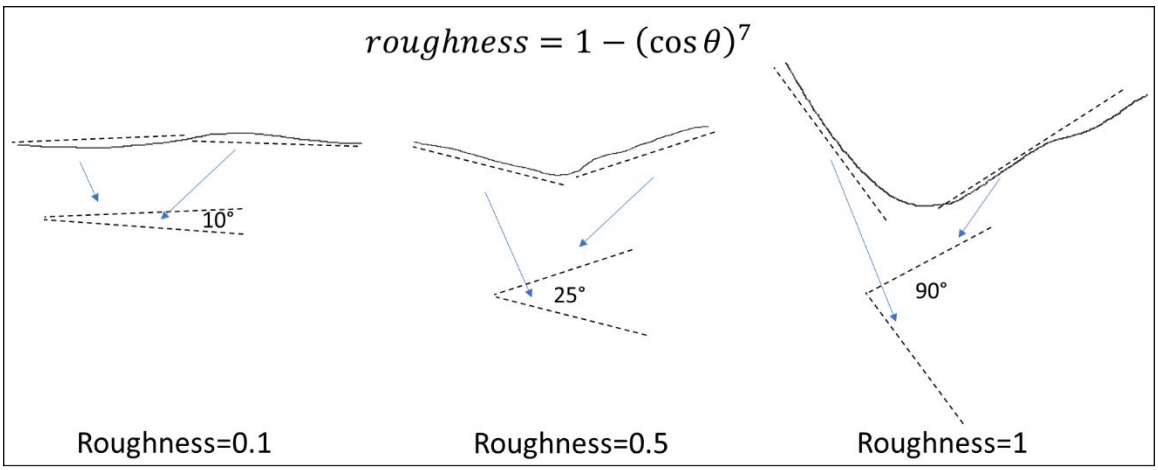


**Figure E4: Roughness measures for different angles of neighboring trendlines**: Example of different roughness values for different skeleton lines (solid lines) shown in two dimensions. Neighboring trendlines are computed and re-drawn side-by-side to illustrate roughness calculation.

***Curviness***

As stated above, tortuosity can be used to quantify the straightness of a path which we named "**curviness**". However, tortuosity is affected by small direction changes of a path which are quantified by our measure of roughness. By subtracting the impact of roughness from the calculated tortuosity of an airway path, we remain with a value for just the gradual and permanent curviness of an airway:

$$C = T - f(R)$$

Where C is curviness, T is tortuosity, R is roughness and f is an unknown function of roughness. This equation still has two unknowns: C and $f(R)$, so a data fit cannot be easily performed. To overcome this, we must determine values of C and $f(R)$ from experimental data. The simplest method it to set C to 0, meaning zero curviness. This corresponds to macroscopically straight airway, such as the ones presented in Figure E6A. The formula then becomes:

$$T = f(R)$$

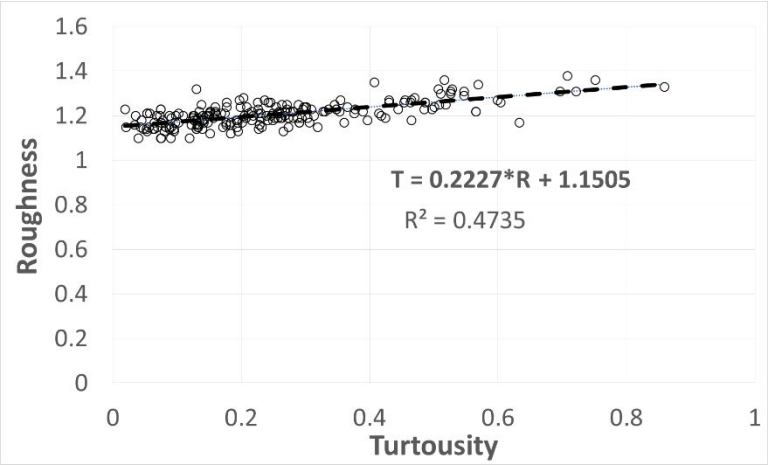


**Figure E5: Correlation between tortuosity and roughness of straight airways**: The linear regression equation for the relationship between tortuosity and roughness can be used to nullify the effects of roughness on Tortuosity. Data was taken from 202 straight airways collected from 22 tissue samples with varying degrees of roughness (higher roughness corresponding to a larger number of fine bumps).

As shown in Figure E5, data from 202 completely straight airways from a sample of 22 tissue samples was used to determine $f(R)$ based in a linear fit. The linear regression formula of the data was used in our formula for curviness:

$$C = T - f(R)$$

$$C = T - 1.15 - 0.223 * R$$

This equation can describe the curviness of all airways using information from the data for only straight airways, as the purpose of the fit was to nullify the effects of roughness on tortuosity. Theoretically, a straight airway path would have a calculated Tortuosity of 1, which should result in a curviness of 0. However, based on the constant in the new formula of 1.15, the curviness for a perfectly straight "theoretical" airway would be -0.15. The additional -0.15 in the constant is due to small pixel based "bumps" of the skeleton caused by the discrete nature of voxels at the pixel limit of images. Figure E6(A-D) provides examples of different skeleton lines from airways with different degrees of roughness and curviness. The fine zig-zagging of the skeleton lines at the pixel level leads our data to the possibility of minor negative values for curviness as shown in Figure E6B. Such values can be attributed to imperfections in the image resolution, which have not been found to tangibly skew data.

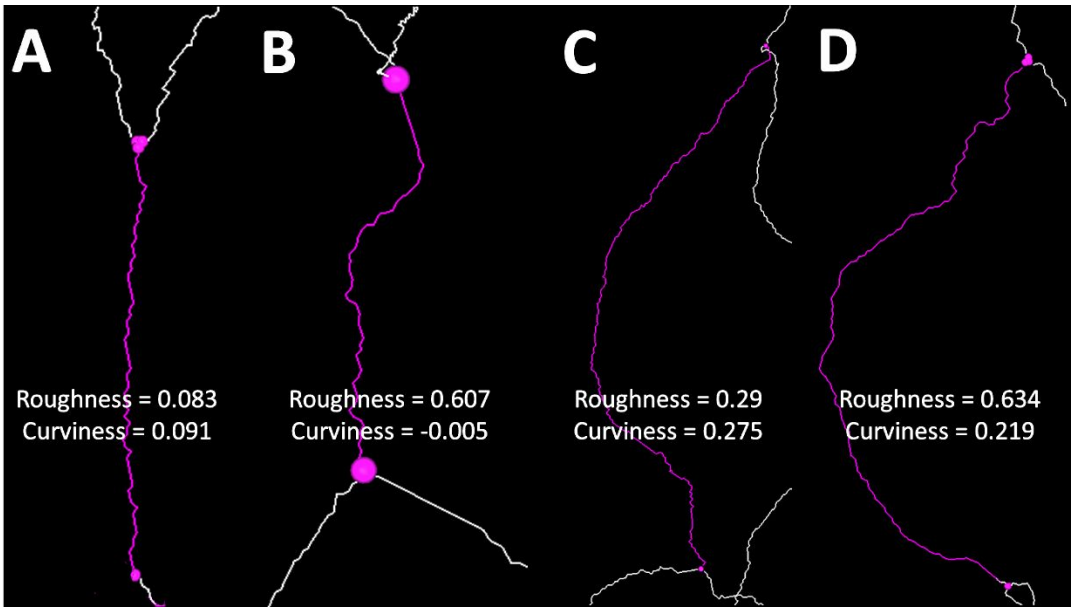


**Figure E6: Examples of the four distinct types of airways**: The four types of individual airway skeleton lines depicted here correspond to the four theoretical 'archetypes' from Figure E7. Magenta dots indicate branch points. The roughness and curviness values for each analyzed airway path (magenta) are shown in white text. (A) Example of a straight smooth airway (low roughness and curviness); (B) Example of a straight rough airway because of the central bump but overall straightness; (C) Example of a curved smooth airway (low roughness and a long continuous curve); (D) Example of a curved rough airway (high roughness and high curviness).

***Biological interpretation of roughness and curviness***

The goal of roughness and curviness is to calculate geometric attributes of airways using the skeleton line. Curviness relates to how curved the path of an airway is, excluding small distortions of the airway path which are described by the roughness. An airway can be idealized to have a high or low quality of both of these attributes and an example is given in Figure E7 that describes the four unique 'archetype' airways.

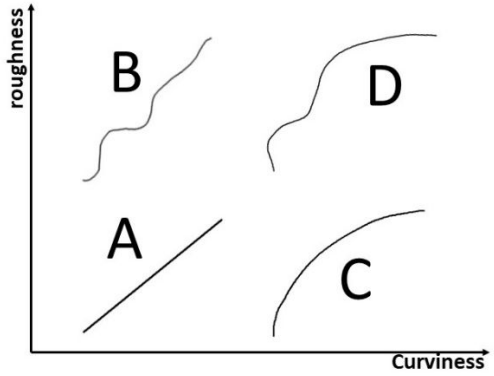


**Figure E7: Four main theoretical archetypes of airway skeletons with different degrees of roughness and curviness.** (A) Example of a smooth and straight airway skeleton (low roughness and low curviness); (B) Rough and straight airway; (C) Smooth and curved airway; (D) Rough and curved airway.

**Stereological quantification of the lung parenchyma in IPF**

Fibrosis, inflammation, edema and atelectasis in the IPF lung leads to impairment of gas exchange. To enable an objective differentiation of parenchyma that still contributes to gas exchange and parenchyma that is not aerated due to extensive remodeling, we followed a recently proposed classification of the parenchyma into two main groups: aerated and non-aerated(3). The diagram in Figure E8 shows the general parenchymal sub-types. This classification was used for the stereology based point counting described by Figure E9. The line intercept and point counts were used to calculate the lung structure measurements by sample and by subject using previously published formulas(3, 4).

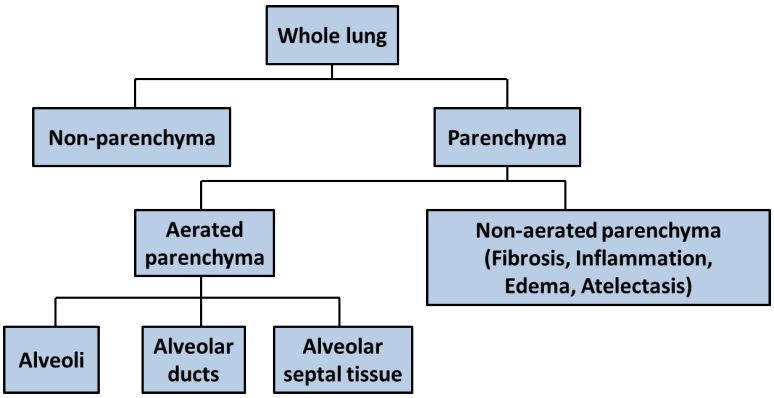


**Figure E8:** Diagram of the stratification implemented for differentiating lung parenchyma sub-types for the stereological assessment at the microCT level.

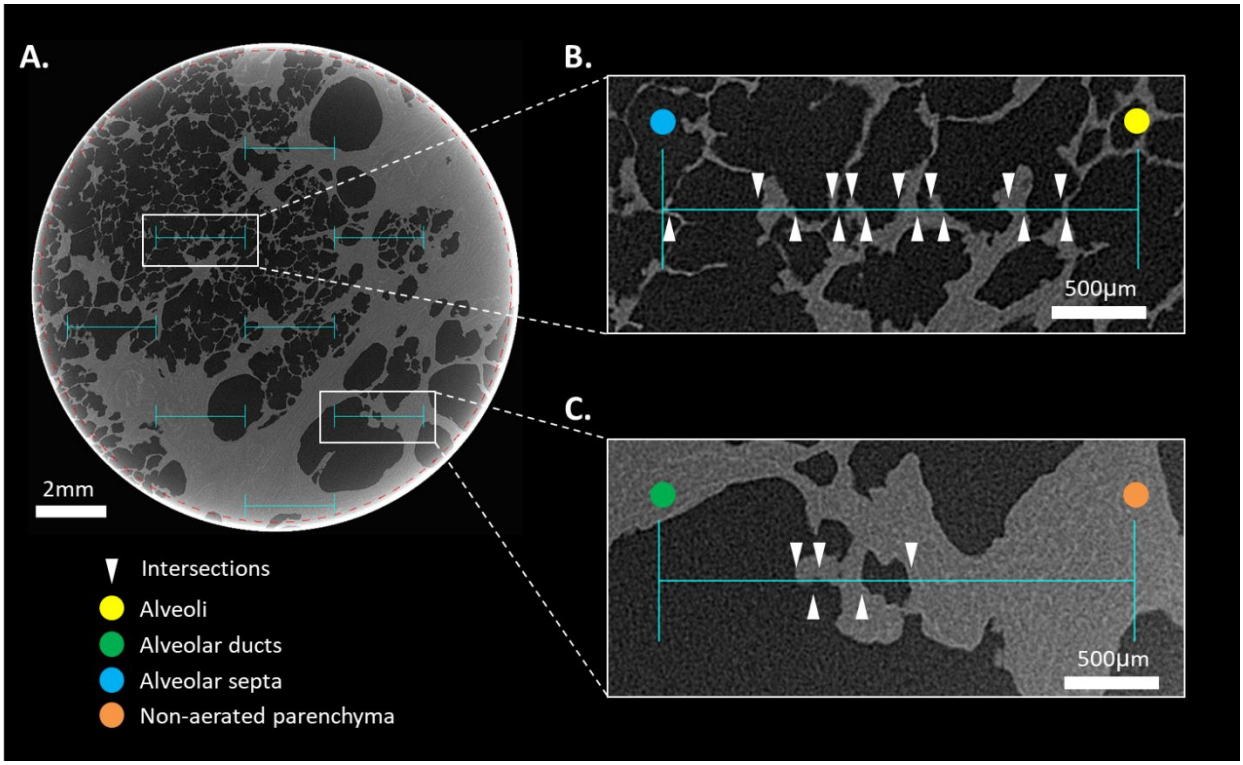


**Figure E9: Stereological counting probes applied to microCT image**
(A) Example microCT images from an IPF sample is shown with a checkered-pattern line-grid (line length of 2.5 mm) that was randomly overlaid on all images using a custom software developed in the lab. Scale bar is 2mm. (B) and (C) The line intercepts are counted and end points are highlighted depending on the type of parenchymal feature the end-point falls on. A legend of the color-coding is provided in the figure. Scale bars are 500µm.

Table E2: MicroCT analysis data per case (IPF cases)

| **IPF Case** | **1** | **2** | **3** | **4** | **5** | **6** | **7** | **8** | **Mean ± SD** |
|---|---|---|---|---|---|---|---|---|---|
| **Lung side** | L | L | L | L | L | L | L | L | **8L** |
| **Age , years** | 63 | 63 | 65 | 56 | 52 | 63 | 64 | 60 | **61 ± 5** |
| **Pack-years** | 0 | 0 | 30 | 35 | 45 | 40 | 20 | 0.3 | **21 ± 19** |
| **Total lung volume, ml** | 840 | 895 | 1733 | 1571 | 1641 | 957 | 1837 | 1121 | **1324 ± 411** |
| **Lm , µm** | 277 | 321 | 515 | 492 | 333 | 416 | 385 | 293 | **379 ± 89** |
| **Alveolar surface density, 1/cm** | 96 | 78 | 55 | 55 | 89 | 54 | 68 | 96 | **74 ± 18** |
| **Alveolar surface area, $m^2$** | 6.5 | 4.5 | 8.4 | 7.2 | 11.9 | 2.8 | 10.0 | 9.5 | **7.6 ± 3.0** |
| **Vv(alv/par), %** | 38.3 | 26.8 | 24.5 | 26.5 | 47.9 | 15.8 | 34.0 | 48.7 | **32.8 ± 11.6** |
| **Vv(duct/par), %** | 17.6 | 16.3 | 37.0 | 31.7 | 12.9 | 14.9 | 21.6 | 13.2 | **20.6 ± 9.0** |
| **Vv(septa/par), %** | 28.3 | 26.1 | 27.1 | 28.1 | 24.0 | 23.9 | 28.9 | 30.1 | **27.1 ± 2.2** |
| **Vv(non-aerated par/par), %** | 15.8 | 30.8 | 11.4 | 13.7 | 15.2 | 45.3 | 15.5 | 8.0 | **19.5 ± 12.4** |
| **Vv(tissue/par), %** | 44.1 | 56.9 | 38.5 | 41.8 | 39.3 | 69.3 | 44.4 | 38.0 | **46.5 ± 11.0** |
| **Septal wall thickness, µm** | 70 | 96 | 107 | 118 | 59 | 160 | 101 | 61 | **97 ± 34** |
| **TB per lung** | 1470 | 1645 | 1023 | 2056 | 1109 | 726 | 1985 | 2325 | **1542 ± 562** |
| **TrB per lung** | 2616 | 3055 | 1887 | 3399 | 1895 | 1273 | 3187 | 4055 | **2671 ± 928** |
| **TB branch length, mm** | 2.96 | 3.02 | 2.91 | 2.49 | 3.66 | 3.19 | 3.26 | 2.54 | **3.00 ± 0.38** |
| **TB lumen area, $mm^2$** | 1.24 | 0.81 | 0.51 | 0.51 | 1.42 | 0.44 | 1.11 | 0.79 | **0.85 ± 0.37** |
| **TB lumen diameter, mm** | 1.06 | 0.95 | 0.74 | 0.77 | 1.25 | 0.64 | 1.15 | 0.98 | **0.94 ± 0.21** |
| **TB lumen circularity** | 0.94 | 0.91 | 0.90 | 0.94 | 0.93 | 0.88 | 0.91 | 0.92 | **0.92 ± 0.02** |
| **TB lumen roundness** | 0.78 | 0.76 | 0.74 | 0.79 | 0.76 | 0.74 | 0.72 | 0.74 | **0.75 ± 0.02** |
| **TB wall area, $mm^2$** | 0.86 | 1.06 | 0.76 | 0.69 | 0.90 | 1.45 | 0.98 | 0.55 | **0.91 ± 0.27** |
| **TB wall thickness, µm** | 224 | 340 | 311 | 246 | 217 | 529 | 264 | 178 | **289 ± 110** |
| **TB CV of wall thickness** | 0.18 | 0.21 | 0.17 | 0.21 | 0.17 | 0.21 | 0.20 | 0.14 | **0.19 ± 0.03** |
| **TB branch roughness** | 0.33 | 0.26 | 0.24 | 0.27 | 0.35 | 0.35 | 0.21 | 0.31 | **0.29 ± 0.05** |
| **TB branch curviness** | 0.099 | 0.050 | 0.032 | 0.046 | 0.087 | 0.059 | 0.048 | 0.049 | **0.059 ± 0.023** |

Table E3 MicroCT analysis data per case (Control cases)

| Control Case | 1 | 2 | 3 | 4 | 5 | 6 | 7 | 8 | Mean ± SD |
|---|---|---|---|---|---|---|---|---|---|
| **Lung side** | R | R | L | R | R | R | R | L | **6R 2L** |
| **Age, years** | 56 | 64 | 53 | 77 | 61 | 64 | 65 | 42 | **60 ± 10** |
| **Pack-years** | 0 | 15 | 0 | 0 | 0 | NA | 15 | 15 | **6 ± 19** |
| **Total lung volume, ml** | 2313 | 4080 | 3701 | 2968 | 3611 | 3281 | 3131 | 3401 | **3310 ± 533** |
| **Lm, µm** | 325 | 357 | 346 | 313 | 335 | 430 | 366 | 321 | **349 ± 37** |
| **Alveolar surface density, 1/cm** | 247 | 269 | 278 | 307 | 239 | 186 | 262 | 299 | **261 ± 38** |
| **Alveolar surface area, $m^2$** | 50.2 | 97.6 | 93.6 | 79.2 | 76.7 | 51.9 | 73.1 | 91.4 | **76.7 ± 18.0** |
| **Vv(alv/par), %** | 51.8 | 70.5 | 70.9 | 75.7 | 67.1 | 56.7 | 71.6 | 70.0 | **66.8 ± 8.2** |
| **Vv(duct/par), %** | 27.6 | 13.3 | 12.8 | 9.0 | 12.3 | 27.4 | 11.2 | 10.8 | **15.5 ± 7.5** |
| **Vv(septa/par), %** | 20.6 | 16.2 | 16.3 | 15.3 | 20.6 | 15.9 | 17.2 | 19.2 | **17.7 ± 2.2** |
| **Vv(non-aerated par/par), %** | 0.0 | 0.0 | 0.0 | 0.0 | 0.0 | 0.0 | 0.0 | 0.0 | **0.0 ± 0.0** |
| **Vv(tissue/par), %** | 20.6 | 16.2 | 16.3 | 15.3 | 20.6 | 15.9 | 17.2 | 19.2 | **17.7 ± 2.2** |
| **Septal wall thickness, µm** | 17 | 12 | 12 | 10 | 17 | 17 | 13 | 13 | **14 ± 3** |
| **TB per lung** | 3833 | 8907 | 6709 | 10057 | 9428 | 3191 | 10372 | 13203 | **8212 ± 3414** |
| **TrB per lung** | 7534 | 18355 | 13634 | 22308 | 17466 | 5637 | 21847 | 27363 | **16768 ± 7471** |
| **TB branch length, mm** | 2.42 | 2.23 | 2.53 | 1.46 | 2.48 | 3.71 | 2.14 | 2.20 | **2.40 ± 0.63** |
| **TB lumen area, $mm^2$** | 0.32 | 0.29 | 0.27 | 0.16 | 0.18 | 0.54 | 0.16 | 0.28 | **0.28 ± 0.12** |
| **TB lumen diameter, mm** | 0.65 | 0.62 | 0.59 | 0.46 | 0.48 | 0.84 | 0.45 | 0.61 | **0.59 ± 0.13** |
| **TB lumen circularity** | 0.92 | 0.96 | 0.94 | 0.95 | 0.95 | 0.94 | 0.96 | 0.96 | **0.95 ± 0.01** |
| **TB lumen roundness** | 0.76 | 0.81 | 0.77 | 0.78 | 0.78 | 0.77 | 0.77 | 0.84 | **0.79 ± 0.03** |
| **TB wall area, $mm^2$** | 0.20 | 0.09 | 0.11 | 0.08 | 0.11 | 0.26 | 0.11 | 0.10 | **0.13 ± 0.06** |
| **TB wall thickness, µm** | 88 | 50 | 41 | 56 | 55 | 74 | 52 | 53 | **59 ± 15** |
| **TB CV of wall thickness** | 0.13 | 0.06 | 0.18 | 0.17 | 0.16 | 0.16 | 0.09 | 0.12 | **0.14 ± 0.04** |
| **TB branch roughness** | 0.22 | 0.15 | 0.13 | 0.16 | 0.10 | 0.16 | 0.14 | 0.16 | **0.15 ± 0.04** |
| **TB branch curviness** | 0.027 | 0.027 | 0.030 | 0.047 | 0.028 | 0.023 | 0.062 | 0.033 | **0.035 ± 0.013** |

**References:**


1. Alberca AS. Tangent line and normal plane to a trajectory in the space – GeoGebra. *Date Accessed 2021-02-19* at <https://www.geogebra.org/m/Q2C7EfBn>.

2. Jones MD, Long J. Tortuosity as a metric for evaluating branch motion paths under dynamic loading. *Proc - 2012 IEEE 4th Int Symp Plant Growth Model Simulation, Vis Appl PMA 2012* 2012. p. 172–179.doi:10.1109/PMA.2012.6524830.

3. Lutz D, Gazdhar A, Lopez-Rodriguez E, Ruppert C, Mahavadi P, Günther A, Klepetko W, Bates JH, Smith B, Geiser T, Ochs M, Knudsen L. Alveolar derecruitment and collapse induration as crucial mechanisms in lung injury and fibrosis. *Am J Respir Cell Mol Biol* 2015;52:232–243.

4. Vasilescu DM, Phillion AB, Kinose D, Verleden SE, Vanaudenaerde BM, Verleden GM, Van Raemdonck D, Stevenson CS, Hague CJ, Han MK, Cooper JD, Hackett TL, Hogg JC. Comprehensive stereological assessment of the human lung using multiresolution computed tomography. *J Appl Physiol* 2020;128:1604–1616.